Electronic Supplementary Information (ESI)

Immobilizing Ni nanoparticles to mesoporous silica with size and location control via a polyol-assisted route for coking- and sintering-resistant dry reforming of methane

Ting Xie, Liyi Shi, Jianping Zhang and Dengsong Zhang*

Research Center of Nano Science and Technology, Shanghai University, Shanghai 200444, China.

Fax: +86-21-66136079; Tel: +86-21-66136081; E-mail: dszhang@shu.edu.cn

Experimental Section:

1. Preparation of catalysts

a. Synthesis of SBA-15.

SBA-15 silica was synthesized as reported by Zhao et al. [s1] 4.0 g of Pluronic P123 was dissolved in30mLof deionized water and 120 mL of 2 M HCl solution, the resulting mixture was stirred for about 15min until the solution became transparent. Then, 8.50 g of TEOS was added dropwise, and kept stirring at 40℃.After 24h,the mixture was transferred into an autoclave for further reaction at 100℃ for 24h.The solid product was collected by filtering, and washed with water and ethanol for several times. Subsequently dried the sample at 100℃，and calcined at 550℃ for 6hto remove the surfactant.

b. Synthesis of the series of Ni/SBA-15 catalysts.

The Ni/SBA-15 catalysts were synthesized by a modified impregnation method employing different kinds of solvent. Briefly, 0.27 g nickel nitrate hexahydrate and 0.5 g SBA-15 were dissolved in 10mL deionizedwater, ethanol, ethylene glycol and glycerol (the obtained catalysts were noted as Ni/SBA-15-H_2O, Ni/SBA-15-EA, Ni/SBA-15-EG and Ni/SBA-15-GC, respectively, and then stirred overnight and subsequently dried in vacuum till the solvent completely volatilized. Lastly, we obtained the product via the calcination at 550 ^oC for 4 h in N_2, another 2 h in air and the *in-situ* reduction at 750 ^oC for 1 h by H_2-TPR.

2. Characterization

The morphologies were observed by a TEM (JEOL JEM-200CX). The high-resolution transmission electron microscopy (HRTEM) and high angle annular dark field scanning transmission electron microscopy (HAADF-STEM) were conducted to characterize the detailed morphology of catalysts employing a JEM-2100F TEM 200 kV. The microscope was also fitted with a liquid nitrogen cooled EDS detector for elemental analysis. The Ni particle size distribution is calculated by Nano Measurer.

The H_2-TPR measurements were carried out in a quartz tube reactor equipped with a thermal conductivity detector (TCD). First of all, the catalysts (80 mg) were pretreated at 300 ^oC for 30 min in a flowing stream of high-purity nitrogen. After cooling to room temperature, a 10 % H_2 of N_2 gas mixture (40mL/min) was introduced and the programing temperature was controlled from room temperature to 850 ^{o}C with a rate of 10 ^{o}C·min^{-1}.

The TPO measurements were carried out with the same procedure of H_2-TPR. The difference was that the amount of the used catalysts was 50 mg and a 10 % O_2 of N_2 gas mixture was applied.

TG/TGA (SHIMADZU DTG-60H) was used to investigate the amount of coke formation on the used catalysts. The temperature was increased from room temperature to 1000 ^{o}C at a rate of 10 ^{o}C·min^{-1}.

3. DRM test

The CO_2 reforming of methane reactions was carried out in a fixed bed reactor with a quartz tube (inner diameter of 8 mm). The quartz tube was filled with 0.12 g of catalysts (40-60 mesh) and fed a mixture of CH_4 and CO_2 (CH_4:CO_2 = 1:1, 15 mL/min per reactor). The catalytic tests were carried out from 450 ^{o}C to 800 ^{o}C with a heating rate of 5 ^{o}C/min. The effluent product gases were cooled in an ice-water bath and analyzed by online gas chromatography with a TCD, using a TDX-01 packed column. The durability tests were also carried out at 750 °C for 1200 min.

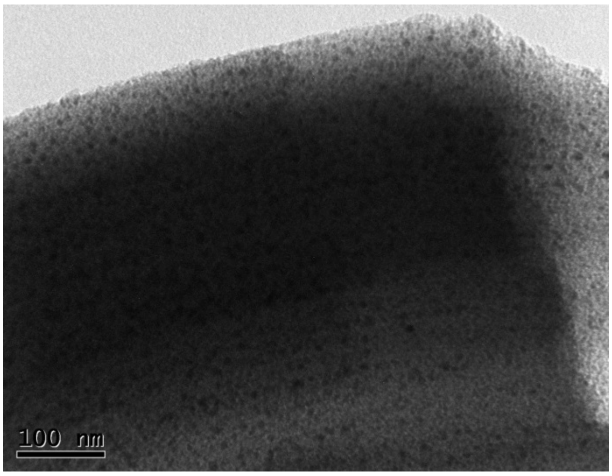

Fig. S1. TEM image of Ni/SBA-15-EG after the step of pyrolysis.

Ethylene glycol decomposes to carbon after the step of pyrolysis (Fig. S1). The mesoporous channels of SBA-15 are not obvious which filled by carbon templates. Meanwhile, the Ni NPs are *in situ* immobilized in the channels without migration and sintering.

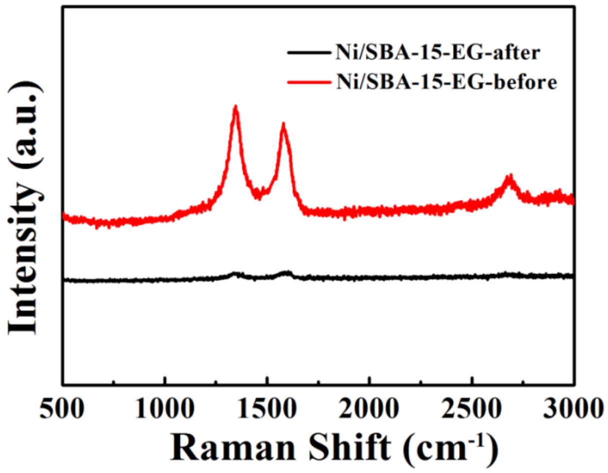

Fig. S2. Raman spectra of the Ni/SBA-15-EG catalyst before and after removing the carbon templates.

The Raman spectra (Fig.S2) exhibits three distinct peaks at 1342, 1580 and 2685 cm^{-1}of Ni/SBA-15-EG before being exposed in air. The 1342 and 1580 cm^{-1}peaks are readily assigned to the D (disorder) and G (graphite) bands of the carbon.[s2] The2685 cm^{-1} band is associated with the overtone of the D band (2×1342 cm^{-1} = 2684 cm^{-1})and indicates a carbonaceous matrix, which derives from the carbonization of ethylene glycol. After being exposed in air, these peaks almost disappear indicating the remove of carbon templates.

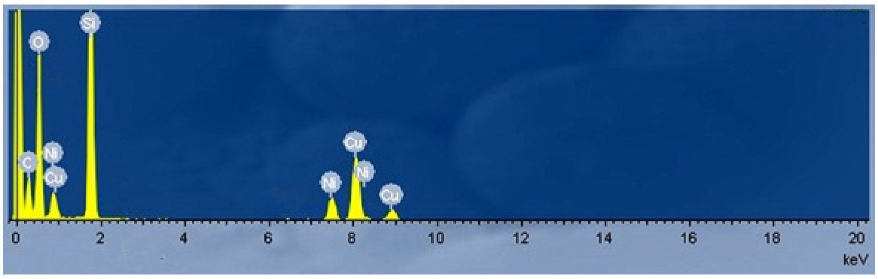

Fig. S3. EDX spectrum for the Ni/SBA-15-EG catalyst.

The EDX spectrum (Fig.S3) reflects the peaks of element C, O, Ni, Si and Cu, the reflection peak of Ni indicates that Ni NPs are successfully loaded on the silica support. The existence of C suggests the residue deriving from the carbonization of EG.

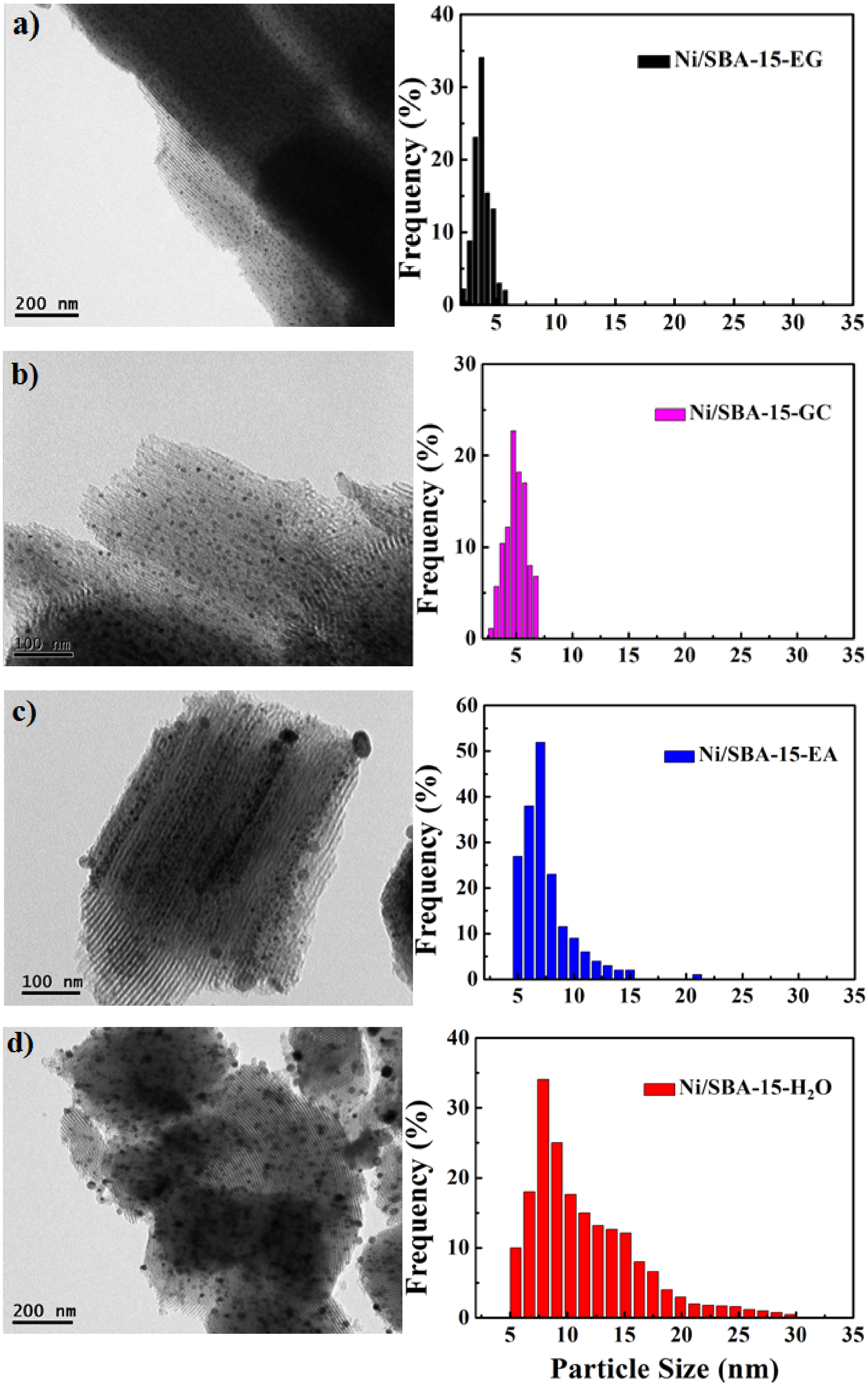

Fig. S4. TEM images and the corresponding Ni Particle size distribution histograms of the catalysts: a) Ni/SBA-15-EG, b) Ni/SBA-15-GC, c) Ni/SBA-15-EA and d) Ni/SBA-15-H_2O.

In the case of Ni/SBA-15-EG (Fig. S4a), Ni NPs are almost anchored into the well-ordered mesoporous channels, indicating that the introduction of EG restricts the location of Ni NPs. It is considerably beneficial to enhancing the sintering-resistance of the catalyst due to the confinement effect arising from the mesoporous wall of silica support. It can be deduced that nickel precursor can be easily delivered into the pore channels of SBA-15 because of the coordination between EG and the Ni^{2+}, resulting in smaller nickel oxide arising from the nickel precursor decomposition.[s3-5] Simultaneously, the carbon template stemming from the carbonization of EG further maintains the high dispersion of nickel species during thermaltreatment.

The micro morphology and Ni particle size distribution of Ni/SBA-15-GC (Fig. S4b) are similar to those of Ni/SBA-15-EGin which Ni NPs have the tiny size and uniform distribution. The tiny size and uniform distribution of Ni NPs in Ni/SBA-15-GC should favor the improvement the activity and stability in the DRM reaction. However, the high viscosity and boiling point of GC may bring trouble to experimental operation such as diffusing and drying, and it may impact on the delivering and immobilizing for Ni NPs.

For the catalyst Ni/SBA-15-EA (Fig. S4c), some Ni particles are loaded inside the pores of silica support with small size, but others are clearly aggregated on the outside surface of SBA-15. The Ni NPs inside of the channels are far smaller than those leaving behind outside because of the confinement effect.[s6] EA can’t deliver all the Ni species into mesoporous channels, it might impute the insufficient alcoholic hydroxyl group and carbon source. The metal particles growth decreases the access to active sites for reactant gases,[s7, 8] and it should directly impact on catalytic performance during DRM reaction.

The TEM micrograph of Ni/SBA-15-H_2O (Fig. S4d) shows that a fraction of pores contains tiny Ni NPs, while other mesoporous channels virtually host no metal particles. A fairly large number of Ni NPs persisting on the external wall of the mesopores generally have bigger size compared with those inserting into the channels. According to the corresponding histogram, the Ni particle-size distribution has a wide range from 4.7nm to 31.5nm, and exhibits a maximum centered at 8-9 nm. The bigger size of nickel particles than the pore diameter further confirms that these Ni NPs haven’t been delivered into the channels of SBA-15. Such an irregular spatial distribution should be a potential hazard to catalytic performance.[s9]

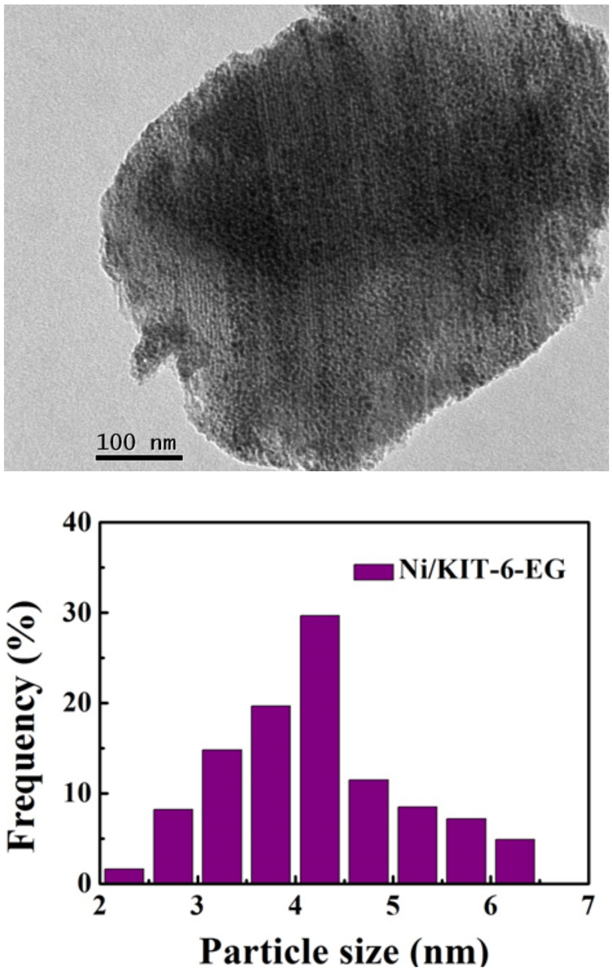

Fig. S5. TEM image and the corresponding Ni Particle size distribution histogram of the catalyst Ni/KIT-6-EG.

The characterization result from the TEM image (Fig. S5) exhibits that the Ni NPs are highly dispersed in the mesoporous channels of KIT-6 with small size about 4.2 nm in average size. It features similarly to the morphology of Ni/SBA-15-EG which benefits from the delivery and immobilization of EG reagent.

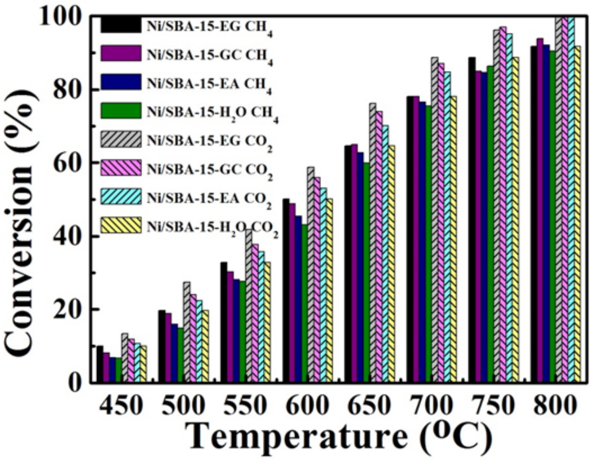

Fig. S6. CH_4 and CO_2 conversions at different temperatures.

The four catalysts prepared with different reagents exhibit different catalytic activities (Fig. S6). The catalyst Ni/SBA-15-EG performs better than Ni/SBA-15-GC, the two catalysts have the higher catalytic activity than the other two Ni/SBA-15-EA and Ni/SBA-15-H_2O, and the catalyst Ni/SBA-15-H_2Oshows the lowest activity. It could be attributed to the tiny and equably dispersed Ni NPs which afford more exposed active sites to the reactant gases in the catalysts Ni/SBA-15-EG.

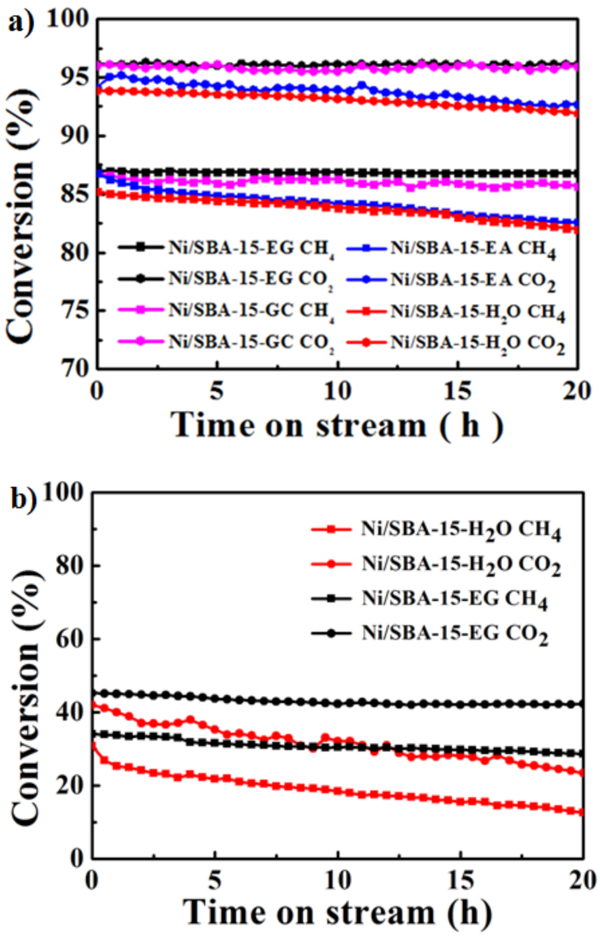

Fig. S7. a) High catalyst conversions *versus* reaction time at 750 °C in the stability test, b) Low catalyst conversions for Ni/SBA-15-EG and Ni/SBA-15-H_2O *versus* reaction time at 750 °C in the stability test. [Catalytic conditions: 200 mg of catalysts and a mixture of CH_4 and CO_2 (CH_4:CO_2 = 1:1, 30 mL/min per reactor)]

Observed from the curves of stability test (Fig. S7a), similar to Ni/SBA-15-EG, the catalyst Ni/SBA-15-GC is durable in the DRM reaction. Whereas, in the case of catalyst Ni/SBA-15-EA, the conversions of both CO_2 and CH_4 decrease with time on stream, indicating the poor stability of this catalyst as similar with that of the catalyst Ni/SBA-15-H_2O. Meanwhile, we also test the stabilities of catalysts Ni/SBA-15-EG and Ni/SBA-15-H_2O with low conversions at 750 ^oC (Fig. S7b). It is also obvious that Ni/SBA-15-EG is more stable than Ni/SBA-15-H_2O.

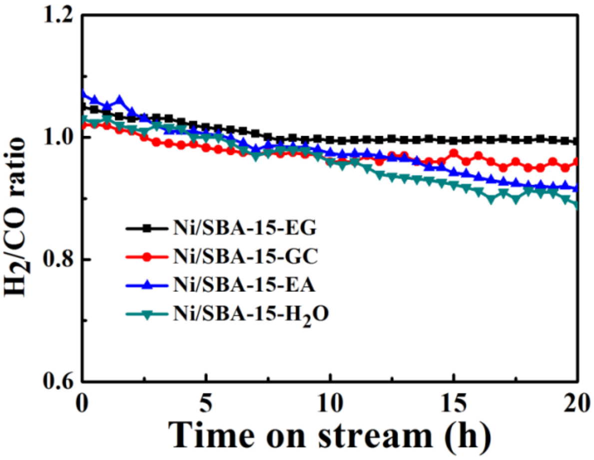

Fig. S8. H_2/CO ratio *versus* reaction time at 750 °C in the stability test.

The H_2/CO ratios of all catalysts (Fig. S8) decrease with time on stream indicating the water-gas shift reaction enhances. Moreover, the Ni/SBA-15-EG has high H_2/CO ratio and behaves more stably because of the more conversions of CH_4/CO_2.[s10]

Table S1 The steady state TOF_{CH4} of various Ni/SBA-15 catalysts during dry reforming of methane at 723K and their variationof activity and dispersion

Sample	Ni loading[a] (wt %)	Ni Dispersion[b] (%)		TOF_{CH4}[c] (h^{-1})		Activity loss (%)
		t=10min	t=480min	t=10min	t=480min	
Ni/SBA-15-EG	6.1	14.1	13	228.5	198.2	13.3
Ni/SBA-15-H_2O	7.4	7.9	5.8	208.4	169.4	18.7
Ni/SBA-15-GC	5.9	13.6	11.7	225.3	193.6	14.1
Ni/SBA-15-EA	6.9	8.7	6.9	216.0	173.4	19.7

[a] Determined by ICP

[b] Determined by H_2 chemsorption

[c] in $mole_{CH4}.h^{-1}.mole^{-1}_{surf.\ Ni}$

The catalyst Ni/SBA-15-EG exhibits higher Ni dispersion (Table S1) indicating the smaller Ni NPs. The initialturnover frequency (TOF) values of CH_4forthe four samples feature similarly, while after 480 min, the TOF values forNi/SBA-15-H_2O and Ni/SBA-15-EA are lower than those for Ni/SBA-15-EG and Ni/SBA-15-GC. The activity losses of Ni/SBA-15-EG and Ni/SBA-15-GC are smaller than those of the other two catalysts, revealing the high stabilities of them.

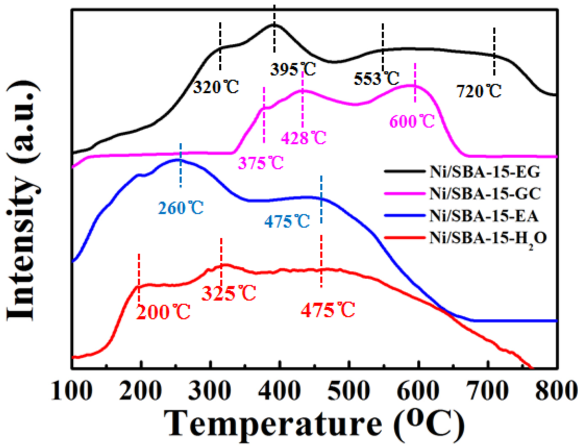

Fig. S9. H_2-TPR profiles of the four fresh catalysts.

As shown in the H_2-TPR profiles (Fig. S9), two reduction peaks of Ni/SBA-15-EA appear at 475^{o}C and 260^{o}C, and it does not display an enhanced interaction between the NiO NPs and silica substrate as compared with Ni/SBA-15-H_2O.Contrary to EA, GC has facilitated reduction behavior of NiO NPs. As a result, a mass of Ni species are reduced at higher temperature region as 428^{o}C and its shoulder peak at 375^{o}C, there is a distinct peak at 600^{o}C assigning to small size Ni NPs confined in the mesoporous channels. The catalyst Ni/SBA-15-EG reflects the H_2consumptionpeak at the highest temperature as 720 ^{o}C, indicating the strongest metal-support interaction.

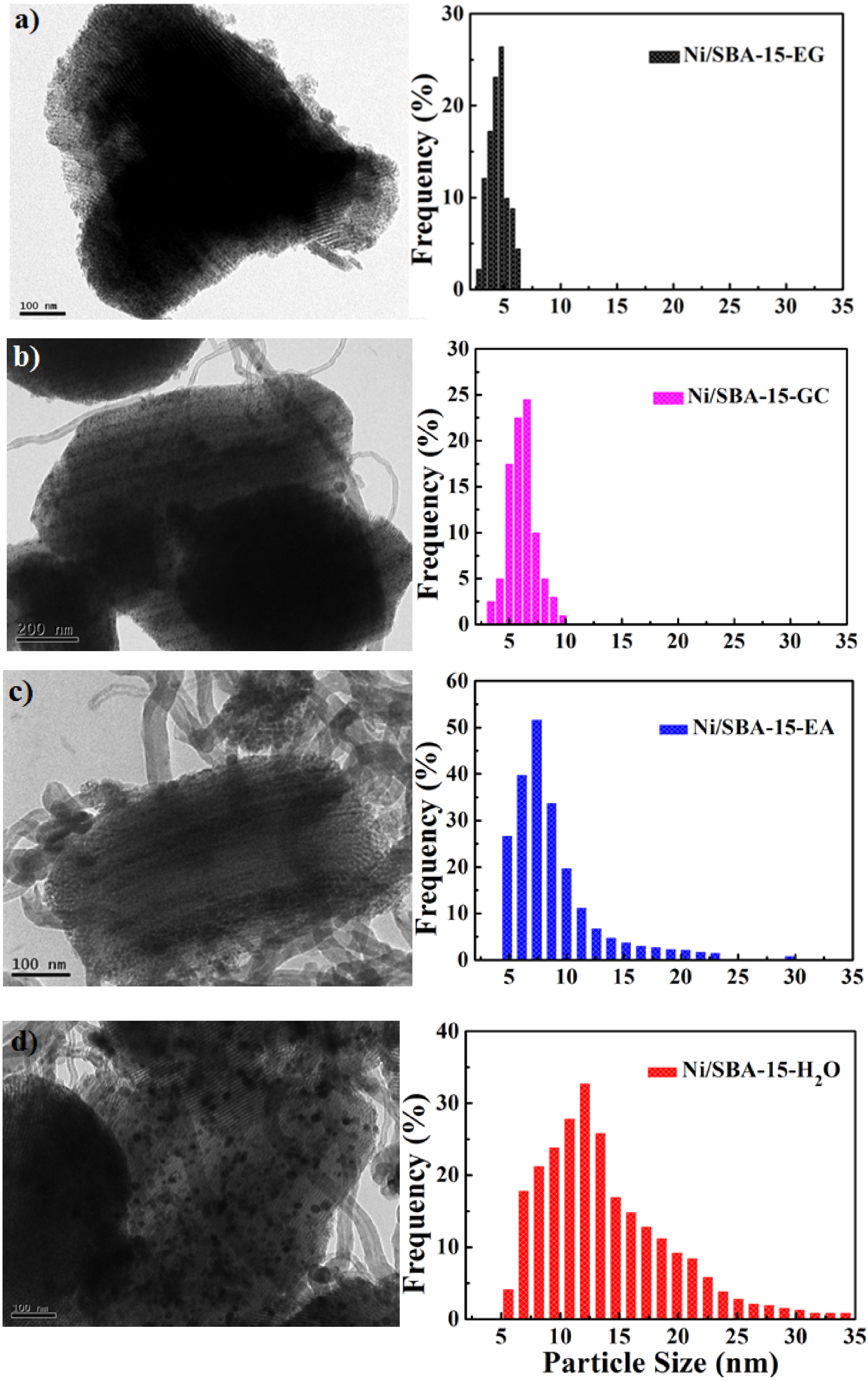

Fig. S10. TEM imagesand the corresponding Ni Particle size distribution histograms of the spent catalysts after the long-term stability test: a) Ni/SBA-15-EG, b) Ni/SBA-15-GC, c) Ni/SBA-15-EA and d) Ni/SBA-15-H_2O.

The TEM image and corresponding histogram of the spent catalyst Ni/SBA-15-EG (Fig. S10a) verify our deduction that the well-ordered mesoporous structure is preserved, and a thin graphene-like layer covers the silica support after the rigorous reaction. The Ni NPs after long-term stability test are maximum centered at 4.7 nm in average size, they haven't changed significantly. The deposited carbonaceous species, especially the carbon nanotubes on the spent catalysts can hardly been observed. It has proved that the small size Ni particles process a higher saturation concentration of carbonaceous species, so it can suppress carbon diffusion through the Ni NPs due to the lower driving force and then avoid the formation of carbon nanotubes.[s11]

The morphology and the corresponding histogram of spent catalyst Ni/SBA-15-GC (Fig. S10b) feature similarly to those of the spent Ni/SBA-15-EG, its mesoporous structure still remains and the aggregation has not occurred on the Ni NPs, about 6 nm in average. A thin graphene-like layer deposits on the silica substrate, and a few of carbon nanotubes generated through the diffusion of deposited carbon.

The TEM image of Ni/SBA-15-EA (Fig. S10c) shows that the well-ordered mesoporous structures are collapsed by the covering of graphene-like coke layers and block of carbon nanotubes.What's more, carbon nanotubes encapsulate the Ni NPs which impact on the interaction between Ni NPs and support silica so that partial Ni particles detach from the support, consequently, the structure of catalyst is destroyed. Most of these carbon nanotubes are curve since that majority of graphite carbon depositing on the Ni NPs diffuses overwhelmingly and unequally.[s12] As shown in the particle size distribution, the sizes of Ni NPs distribute from 3.7 nm to 34 nm, and about 9.1 nm in average, indicating the sintering of Ni NPs.

For catalyst Ni/SBA-15-H_2O (Fig. S10d), the Ni NPs grow bigger, about 13.7 nm in average, and a large amount of carbon species appears after the harsh reaction. The well-ordered mesoporous structure was collapsed by the covering of graphene-like coke layers and block of carbon nanotubes. Generally, three types of carbon exist: intermediate carbonaceous species derive from the CH_4 decomposition, graphite carbon and carbon nanotubes arise from the carbonaceous species nucleation and diffusion. [s13] The graphite carbon is the chief culprit for deactivation of catalysts because it acts like a shell on the catalyst and totally covers the nickel active sites layer by layer.

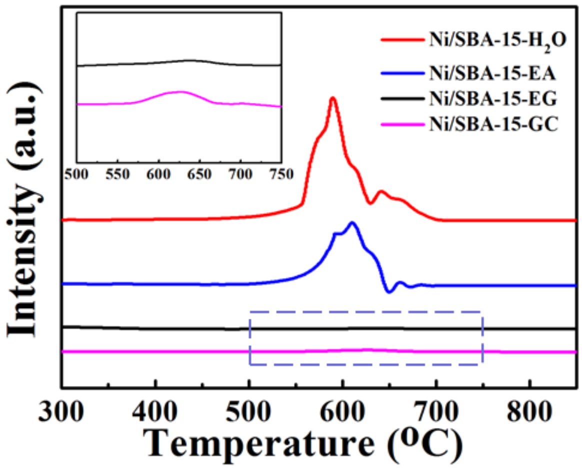

Fig. S11.O_2-TPO profiles of the used catalysts after long-term stability tests (the inset is the enlargement of used Ni/SBA-15-EG and Ni/SBA-15-GC)

The O_2-TPO profile (Fig. S11) shows that Ni/SBA-15-EA exhibits a bit lower peaks assigned to the carbon deposition than Ni/SBA-15-H_2O.While the peaks of CO_2 desorption associated with the amount of coke in catalyst Ni/SBA-15-EG and Ni/SBA-15-GC can't be detected compared with that of the coke in Ni/SBA-15-EA and Ni/SBA-15-H_2O.The inset displays the lower CO_2 peak of Ni/SBA-15-EG than that of Ni/SBA-15-GC, indicating the enhanced coking-resistance of catalyst Ni/SBA-15-EG.

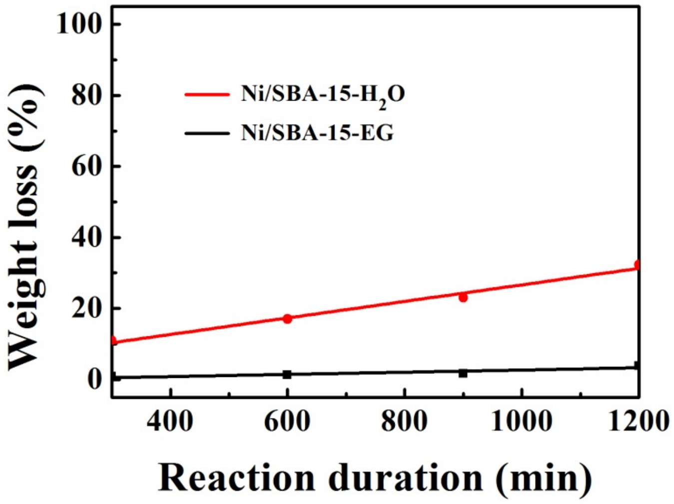

Fig. S12. Coke deposition rate on catalysts Ni/SBA-15-EG and Ni/SBA-15-H_2O.

We have tested the amount of coke deposition on the catalysts Ni/SBA-15-EG and Ni/SBA-15-H_2O at different times (Fig. S12). It shows that Ni/SBA-15-H_2O has larger amount of coke deposition and higher coke deposition rate, indicating the shorter life time compared with Ni/SBA-15-EG.

References

[s1]. D. Y. Zhao, J. L. Feng, Q. S. Huo, N. Melosh, G. H. Fredrickson, B. F. Chmelka, G. D. Stucky, *Science*, 1998, **279**, 548-552.

[s2]. A. R. McFarlane, I. P. Silverwood, E. L. Norris, R. M. Ormerod, C. D. Frost, S. F. Parker and D. Lennon, Chem Phys, 2013, 427, 54-60.

[s3]. J. Chen, Y. Zhang, L. Tan, Y. Zhang, *Ind Eng Chem Res*, 2011, **50**, 4212-4215.

[s4]. Z. Qu, W. Huang, S. Zhou, H. Zheng, X. Liu, M. Cheng, X. Bao, *J Catal*, 2005, **234**, 33-36.

[s5]. Y. Zhang, K. Hanayama, N. Tsubaki, *Catal Commun*, 2006, **7**, 251-254.

[s6]. J. R. Sietsma, J. D. Meeldijk, J. P. den Breejen, M. Versluijs-Helder, A. J. van Dillen, P. E. de Jongh and K. P. de Jong, *Angew. Chem. Int. Ed.*, 2007, **46**, 4547-4549.

[s7]. L. Xu, H. Song, L. Chou, *Appl. Catal., B*, 2011, **108-109**, 177-190.

[s8]. J. Zhu, X. Peng, L. Yao, D. Tong and C. Hu, *Catal. Sci. Technol.*, 2012, **2**, 529.

[s9]. T. V. Choudhary and V. R. Choudhary, *Angew. Chem. Int. Ed.*, 2008, **47**, 1828-1847.

[s10]. B.-Q. Xu. J-M. Wei, J-L. Li, Z-X. Cheng, Q-M. Zhu, *Appl. Catal., A*, 2000, **196**, L167-L172.

[s11]. K. P. De Jong , J. W. Geus, *Catal. Rev*, 2000, **42**, 481-510.

[s12]. X. Yu, N. Wang, W. Chu, M. Liu, *Chem Eng J*, 2012, **209**, 623-632.

[s13]. M. C. J. Bradford, M. A. Vannice, *Catal. Rev*, 1999, **41**, 1-42.